Atomic interfacial charge and energy transfer paths at MoS₂/Pd bonded defect-rich BiOCl interfaces for efficient photocatalysis

Bingjie Sun [a,1], Cheng Huang [b,1], Chenyu Yang [a,1], Da Ke [a], Ye Liu [c], Qi Lu [a], Xiufan Liu [d], Xuyang Xiong [a,*], Yuanzhen Chen [e], Qingqing Jiang [b], Juncheng Hu [b,*], Tengfei Zhou [a,*]

[a] Institutes of Physical Science and Information Technology, Key Laboratory of Structure and Functional Regulation of Hybrid Material (Ministry of Education), Anhui University, Hefei 230601, China
[b] Key Laboratory of Catalysis and Energy Materials Chemistry of Ministry of Education, South-Central University for Nationalities, Wuhan 430074, China
[c] Institut für Chemie and IRIS Adlershof, Humboldt-Universität zu Berlin, Brook-Taylor-Strasse 2, 12489 Berlin, Germany
[d] Hubei Key Laboratory of Pollutant Analysis and Reuse Technology, College of Chemistry and Chemical Engineering, Hubei Normal University, Huangshi 435002, China
[e] State Key Laboratory for Mechanical Behavior of Materials, School of Materials Science and Engineering, Xi'an Jiaotong University, Xi'an, 710049, China

ARTICLE INFO

ABSTRACT

Construction of heterogeneous transmission interfaces that spatially separate Coulomb-bound electron-hole pairs in semiconductors allows exceptional control over optoelectronic properties, thereby enhancing the efficiency of solar energy conversion. In this study, we propose an effective photocatalyst for full water splitting named MS/ BOC-x/Pd, comprising atomic layer of MoS₂ bonded to defect-rich BiOCl, and a non-plasmonic Pd oxidation co-catalyst is exclusively assembled on the sides to form a strong electronic coupling and maximize the trapping of holes. The presence of the Mo-S-Bi motif promotes rapid charge migration, resulting in impressive rates of H₂ and O₂ formation (165 and 9.17 µmol g^{-1} h^{-1}, respectively), without the requirement of sacrificial agents or sensitizers. Through experimental and theoretical investigations, we discovered that the occupation of sulfur atoms in oxygen vacancies extends the overlap of surface charges, thereby facilitating the separation of inner/interfacial electron-hole pairs. The Mo-S-Bi bond provides directional guidance for charge transfer to the surface redox sites. These findings provide valuable insights for the future design of highly efficient photocatalysts for solar energy conversions.

1. Introduction

Converting solar energy to clean fuel is a fascinating yet fundamental topic, as it enables the production of valuable chemicals for industry and feedstocks for moderate artificial synthesis (e.g. N₂ fixation, CO₂ reduction, and environmental remediation) [1,2]. An ideal photocatalyst would have a robust driving force to facilitate the inner separation and migration of photoinduced charge carriers to surface reactive sites [3]. Despite notable progress, photocatalytic energy conversion remains inefficient and rates low, which is explained by the randomly diffusion of electron-holes and sluggish reaction kinetics [4,5]. Considerable research effort is currently being directed towards designing spatial electron transfer channels to steer the charge motion and highly active sites to fulfill the overall/half reaction [6–8]. However, simultaneously integrating these two aspects in one photocatalytic system and achieving convincing H₂/O₂ production are still challenging.

Construction of heterogeneous transmission interfaces is promising for high-performance photocatalyst fabrication due to their flexible local compositions, tunable redox capacities, unique interfacial properties and superior capability of promoting charge separation [9]. Consequently, immobilizing Au, Pt, Pd noble metals or transition metal oxides/sulfides in/on photo-reactive semiconductors (TiO₂, CdS, Cu₂O, BiVO₄) has resulted in numerous highly efficient catalytic systems for overall photocatalytic water splitting (PWS) [10]. However, these semiconductor cocatalysts/bases are commonly anisotropic crystallized, resulting in non-directional migration of interior/interfacial photo-excited electrons [11,12]. Additionally, many heterojunction fabrication schemes such as type-I (straddling gap), type-II (staggered gap), and type-III (broken gap) are average statistical models and energy bands [13–16], which limit in-depth understanding of hybrid interfaces

---

at the atomic level. These bottlenecks impaired further optimization and application of photocatalysts for PWS, forcing a rethink in the design and materials used in photocatalysts construction.

The built-in electric field (IEF) can manipulate the maximum transfer of drifted electrons to surface sites, making it an attractive platform in high-efficiency photocatalysts development [17–19]. Previous studies have shown that two-dimensional (2D) bismuth oxychloride (BiOCl) preferred water dissociation to oxygen relying on IEF-triggered charge separation and surface oxygen vacancies (OVs) [20,21]. The OV serve as charge-trapping/donation and molecular adsorption sites, lowering the water activation/transition barriers and enabling water oxidation [22]. Additionally, 2D molybdenum disulfide (MoS_2) has been proposed as a low-cost alternative to platinum (Pt) for hydrogen production, with its triangular edge site widely proposed as the water reduction site [23]. Studies coupling MoS_2 and BiOCl through defect site along the IEF direction are theoretically both satisfied charge transfer dynamics and surface chemical reactions, motivating a rational design of MoS_2-BiOCl-Pd heterogeneous transmission interfaces for overall PWS perspective.

Herein, we present a straightforward approach for constructing MoS_2-BiOCl-Pd junctions. Our design involves the migration of easily accessible and spatially separated electrons towards few-layered MoS_2, which is firmly attached to the top surfaces of BiOCl through defect-orientated bonding within MoS_2-$[Bi_2O_2]$ interphases. This configuration enables the generation of H_2. Additionally, a non-plasmonic Pd oxidation co-catalyst is selectively positioned on the sides to establish a strong electronic coupling and enhance hole trapping, thereby leading to an increased O_2 formation rate and improved solar-to-hydrogen conversion efficiency. A series of photocatalysts named MS/BOC-x were prepared, with x representing the weight percentage of MoS_2 relative to BiOCl in the synthetic procedure. Next, we examined the photocatalytic activity of these MS/BOC-x and their counterparts for PWS to H_2/O_2. MS/BOC-11.5 displayed excellent H_2/O_2 formation rates (165 and 9.17 $\mu mol \cdot g^{-1} \cdot h^{-1}$) under photo-sensitizer free conditions. To further elucidate the mechanism, we conducted comprehensive characterization studies that revealed MoS_2 was coupled with BiOCl through an interfacial Mo-S-Bi bond, resulting in rapid electron-hole separation/migration during use. Density function theory (DFT) calculations confirmed that the substitution of oxygen by sulfide atoms promoted surface charge accumulation, significantly strengthening the Mo-S bond and guiding charge migration to water-splitting sites.

2. Experimental section

2.1. Materials

2.1.1. Preparation of the defective-rich BiOCl (d-BOC) catalysts

BiOCl nanosheets were firstly synthesized through a hydrothermal method (Details can be found in the supplementary material). Subsequently, the as-synthesized BiOCl nanosheets were treated in Ar atmosphere at 200 °C for 1–3 h in a tube furnace (OTF-1200X, MTI Corporation) respectively, yielding series of defective-rich BiOCl catalysts. (donated herein as d-BOC-1 ~ d-BOC-3).

Preparation of the MoS_2 atomic layers bonded defective BiOCl (MS/BOC-x) catalysts.

An OV-related self-assemble strategy was performed to immobilize MoS_2 atomic layers onto defective BiOCl. Firstly, 6 mg of the as-obtained MoS_2 atomic layers catalyst was dispersed in 75 mL of distilled water under ultrasonication to give a uniform solution A. 60 mg of d-BOC-3 was dispersed in a three-neck flask containing 180 mL of distilled water under ultrasonication as solution B. Solution A and B were respectively deoxygenated by bubbling argon gas for 30 min. Then the solution A was drop-wisely added (1.8–2 mL·min^{-1}) into solution B with continuously stirring at ambient conditions. The above mixture was also deoxygenated by bubbling argon gas (200–220 mL·min^{-1} by a mass flow controller) for 30 min (at room temperature), and then refluxed at 80 °C

for 2 h. Finally, the target products were centrifuged at 500 rpm for 1–2 min to remove the large-aggregated precipitate, and further centrifuged at 3000 rpm for 4–5 min to collect the MS/BOC–x nanosheets. Herein,.x represents the weight percentage of MoS_2 relative to BiOCl in the synthetic procedure ($x = 2.5\%, 5\%, 7.5\%, 11.5\%, 12.5\%, 15\%$).

2.1.2. Preparation of the Pd nano-cubes modified BOC and MS/BOC–11.5

Typically, Pd nanocubes were selectively loaded on the side surface of BiOCl (010/110) nanosheets and MS/BOC–11.5 through a hydrothermal method with the assistance of polyvinyl pyrrolidone (PVP) as a facet-control agent. Excessive PVP was removed with ethanol and deionized water by washing/centrifuging several times (> 5) at 700 rpm for 1–2 min

2.1.3. Characterization

Scanning electron microscopy (SEM) was performed on a field emission scanning electron microscope (Hitachi SU-8010, Japan) operated at a deacceleration voltage of 1.5 kV to characterize the morphologies of the products. Transmission electron microscopy (TEM) images were collected on a JEOL JEM-2010 LaB$_6$ high-resolution transmission electron microscope operated at 200 kV. High-resolution (HRTEM) images were collected on a JEOL JEM-2100 F field-emission high-resolution transmission electron microscope operated at 200 kV. X-ray diffraction (XRD) patterns were recorded on a D8 Advance X-ray diffractometer (Bruker AXS, Germany) equipped with Cu-Kα radiation. Raman spectroscopy was carried out on a confocal laser micro-Raman spectrometer (Thermo DXR Microscope, USA). The laser had a 633 nm wavelength at 5 mW. The X-ray photoelectron spectroscopy (XPS) measurements (VG Multilab 2000 photoelectron spectrometer) used Al Kα radiation as the excitation source under a vacuum of 2×10^{-6} Pa. Photoluminescence (PL) measurements were recorded on a Hitachi F-7000 Fluorescence Spectrometer with a steady-state 150 W xenon lamp as the excitation source ($\lambda = 320$ nm). The UV–vis diffuse reflectance spectra (DRS) were recorded on a spectrophotometer (Agilent Cary-5000), and $BaSO_4$ was used as the background. The electron paramagnetic resonance (EPR) spectra were recorded at room temperature or 77 K by using a JES FA-200 spectrometer (JEOL, Japan) equipped with a 300 W Xe lamp and a 365 nm cut-off filter. 5,5-dimethyl-1-pyrroline-N-oxide (DMPO, 5 mM/L) was used as a spin trap agent.

2.1.4. Synchrotron X-ray absorption spectroscopy (XAS) measurements

Synchrotron X-ray absorption spectroscopy (XAS) was conducted by the wiggler XAS Beamline (12ID) with a set of Si (311) crystals as the monochromator. Structural parameters (coordination numbers and bond lengths) were obtained by a nonlinear least-squares fitting of the theoretical EXAFS curve to the experimental EXAFS data in R space.

2.1.5. Photoelectrochemical measurements

The photocurrent measurement was conducted by an electro-chemical workstation (IviumStath, The Netherland) in a standard three-electrode system (samples as the working electrodes, Pt foil as the counter electrode, and an Ag/AgCl electrode as the reference electrode) with 0.5 mol·L^{-1} Na_2SO_4 as the electrolyte.

The incident photon-to-current conversion efficiency (IPCE) was investigated by optical filters classified as 365 nm, 1.68 W; 460 nm, 1.35 W; 523 nm, 0.45 W; 660 nm, 1.05 W; 740 nm, 0.705 W; and 940 nm, 0.614 W. The IPCE was calculated through Eq. (1):

$$IPCE = \frac{hcj_{sc}}{\lambda\varphi} \tag{1}$$

where φ is the light intensity, λ is the wavelength, h is the Planck's constant, c is the speed of light, and J_{SC} is the photocurrent density at wavelength λ.

1 mol·L^{-1} NaOH (pH=13.6) was used as the electrolyte for open-circuit voltage decay (OCVD) measurements. The Voc decay curves

were selected/normalized to give the τ values according to Eq. (2), reflecting the average lifetime of the photogenerated carriers within the device:

$$\tau = -\frac{k_{\mathrm{B}}T}{q}\left(\frac{dVOC}{dt}\right)^{-1} \qquad (2)$$

where k_B is the Boltzmann constant, T is the temperature (in Kelvin), and q is the total charge of an electron.

The apparent quantum efficiency (AQY) was investigated by optical filters classified as 365 nm, 0.1 W; 435 nm, 0.1 W; 650 nm, 0.1 W. The AQY was calculated through Eq. (3):

$$AQY = \frac{N_e}{N_p} \times 100\% = \frac{10^9(\nu \times N_A \times K) \times (h \times c)}{(\varphi \times \lambda)} \qquad (3)$$

Where N_e is the total number of electrons transferred by the reaction, N_p is the incident photon number, ν is reaction rate(mol•s^{-1}), N_A is Avogadro's constant(6.02×10^{23} mol^{-1}), K is the number of electrons transferred by the reaction, h is Planck's constant, c is the speed of light, φ is the light intensity, λ is the wavelength.

Photocatalytic overall water splitting tests:

The photocatalytic overall water splitting experiment was carried out in a customized reaction chamber (Perfect-light, China). Prior to the photoreaction, catalyst (10 mg) and H$_2$O (10 mL) were uniformly spread into the reaction chamber and followed by evacuating with a mechanical pump and purging Ar to eliminate air for three times. A xenon lamp (300 C, full arc, Perfect-light, China) was used as the light source, and the photocatalytic system was maintained at room temperature. The gaseous products formed were measured by gas chromatography (GC-9790II, Zhejiang Fuli Analytical Instrument Co., Ltd., China) equipped with thermal conductive detector (TCD) and Molecular sieve-5A column. High purity Ar was served as the carrier gas throughout this experiment. The yields of products were calculated through an external standard method.

2.1.6. Isotope labelling experiments

Isotope tracing experiments were performed using H$_2^{18}$O (97%, *Sigma Aldrich*) as the oxygen source. The reactor was evacuated prior to being injected successively with H$_2^{18}$O. Isotopically labeled compounds were separated and analyzed using an Agilent 7890 A gas chromatography mass spectrometer (GC-MS). The GC-MS signals were collected at $m/z = 36$ for the detection of ^{18}O$_2$.

2.1.7. Computational models

All calculations were performed using the first-principles density of functional theory (DFT) with the exchange-correlation energy function of GGA-PBE. [6,7] The calculations were conducted using CASTEP package in which the ultra-soft pseudopotentials were employed for all atoms with the accuracy set as fine. The energy cutoff of 550 eV and a k-point set of $2 \times 2 \times 1$ was chosen for the calculations, with an SCF tolerance of 1.0×10–5 eV/atom, an energy tolerance of 1.0×10–5 eV/atom, a maximum force of 0.03 eV/ Å, and a maximum displacement of 1.0×10–3 Å.

The (3×3) FeS$_2$-(001) supercell with a three Fe-S layers (contain 48 S atoms and 24 Fe atoms) and a vacauum thickness being larger than 15 Å was used for FeS2 model, the Cu5-FeS2 model was obtained by anchoring a Cu5 cluster on the surface, and the spin was set as "polarized" and "used a formal spin as initial". All models were first well-relaxed via geometry and then used for the energy calculations. All transition state searches were performed by the LST/QST protocol with 10 fragments from the initial state to final state.

The adsorption energy was defined as the following equation.

$$E_{ads} = \mathrm{E}_M^* - (\mathrm{E}^* + \mathrm{E}_M) \qquad (3)$$

where E*$_M$, E$_M$, and E* denote the energies of surface-adsorbed molecule

M, free molecule M, and the bare substrate, respectively.

3. Results and discussion

The synthesis of MS/BOC-x photocatalysts was carried out as depicted in Fig. 1a. Initially, bulk MoS$_2$ was exfoliated into atomic layers (MS) using a lithium intercalation/de-intercalation procedure mediated by hydrothermal treatment [24], during which the thickness of MoS$_2$ was sharply-reduced to atomic level. The X-ray diffraction (XRD) analyses indicated the 2 H phase of MoS$_2$, and the transmission electron microscopy (TEM) exhibited lattice fringes corresponding to the (001) facet (Fig. S1). The lateral spacing of a single MoS$_2$ layer was around 4.6 nm, indicating the stacking of 7–8 at. layers of MoS$_2$ along the [001] direction (Fig. 1b,c) [25]. Meanwhile, BiOCl with defects (d-BOC) was prepared via traditional hydrothermal synthesis, followed by Ar treatment for three different durations (denoted as d-BOC-1, d-BOC-2, and d-BOC-3, corresponding to 1 h, 2 h, and 3 h of Ar treatment) [26,27]. XRD patterns of the as-prepared samples were well-indexed to the tetragonal phase of BiOCl (JCPDS06–0249, a=0.3891 nm, c=0.7369 nm and the number of asymmetric unit z = 2), and TEM results (as well as the corresponding fast Fourier transform (FFT) pattern) showed single-crystal nature with square-like morphology (150–250 nm in width and 25–35 in thickness) (Fig. S2). The surface lattices of the BiOCl nanosheets (d-spacing of 0.27 nm, (110) facet of BiOCl) were at a 90° angle with respect to each other, indicating the top and bottom surfaces of a single BiOCl nanoplate were enclosed by (001) facets, while the four side faces were (110)/(010) facets (Fig. 1d,e). Specifically, the (001) planes of BiOCl were [Bi$_2$–O$_2$]$^{2+}$ terminated whereas MoS$_2$ was S^{2-} exposed [28,29]. The electrostatic interaction between these two layers facilitated easy recombination through Bi-S bonding. Finally, under ultrasonication in an Ar atmosphere, MS and d-BOC-3 were chemically treated to produce the MS/BOC-x photocatalysts (abbreviated as 2.5%, 5%, 7.5%, 11.5%, 12.5%, and 15%). For comparison, several control photocatalysts were also prepared, denoted herein as pristine BiOCl (BOC, OV-quenched d-BOC nanosheets in O$_2$), Pd nano-cubes modified MS/BOC (Pd-MS/BOC-11.5), and a physical mixture of MoS$_2$ and BiOCl (p-MS/BOC, which involved grinding the as-prepared MoS$_2$ and d-BOC-3 powders).

The geometry structures of the MS/BOC-x hybrids were analyzed by TEM tests. Chemically assembled samples showed distinct heterostructures consisting of layered MoS$_2$ uniformly dispersed on BiOCl nanosheets, as shown in Fig. 1f, g, and Fig. S3. The architecture's formation mechanism can be attributed to the ultra-thin feature of two-dimensional (2D) nanomaterials, which tend to aggregate to minimize surface energies and/or neutralize charges [30]. However, physically.

mixed p-MS/BOC displayed irregular morphologies with an ambiguous hierarchical structure, suggesting a weak/random combination of MoS$_2$ with BiOCl species (Fig. S4). The isolated BiOCl and MoS$_2$ retained their basic morphology after physical/chemical treatment, both remaining (001) facet exposure (Fig. S5). To further elucidate the texture information of the MS/BOC-x, Raman spectra of pristine MS, BOC, and MS/BOC–11.5 were selected for comparison. Fig. 2a showed Raman vibration peaks, including A$_1^1$ g external Bi–Cl phonon mode (60 cm^{-1}), A$_1^2$ g internal Bi–Cl phonon mode (145 cm^{-1}), and Eg internal Bi–Cl phonon mode (190 cm^{-1}) of BiOCl. These peaks were scarcely altered after MoS$_2$ loading [31,32], whereas the E$_2^1$ g/A$_1^1$ g peak ratio of MoS$_2$ gradually increased from 35% to 42%. Noted that the A$_1^1$ g out-of-plane Mo–S phonon mode (410 cm^{-1}) was preferentially excited for the edge-terminated structure, and the E$_2^1$ g in-plane Mo–S phonon mode (380 cm^{-1}) was preferentially excited for the terrace-terminated structure [33]. This intensified variation of the E$_2^1$ g Raman vibration indicated the predominant formation of the terrace-to-terrace architecture of MS/BOC-x, with MoS$_2$ atomic layers probably bonded to BiOCl through the [001] direction (Fig. 1f inset).

To further clarify the speculations derived from Raman results, electron spin resonance (ESR) spectra were used to detect defects in
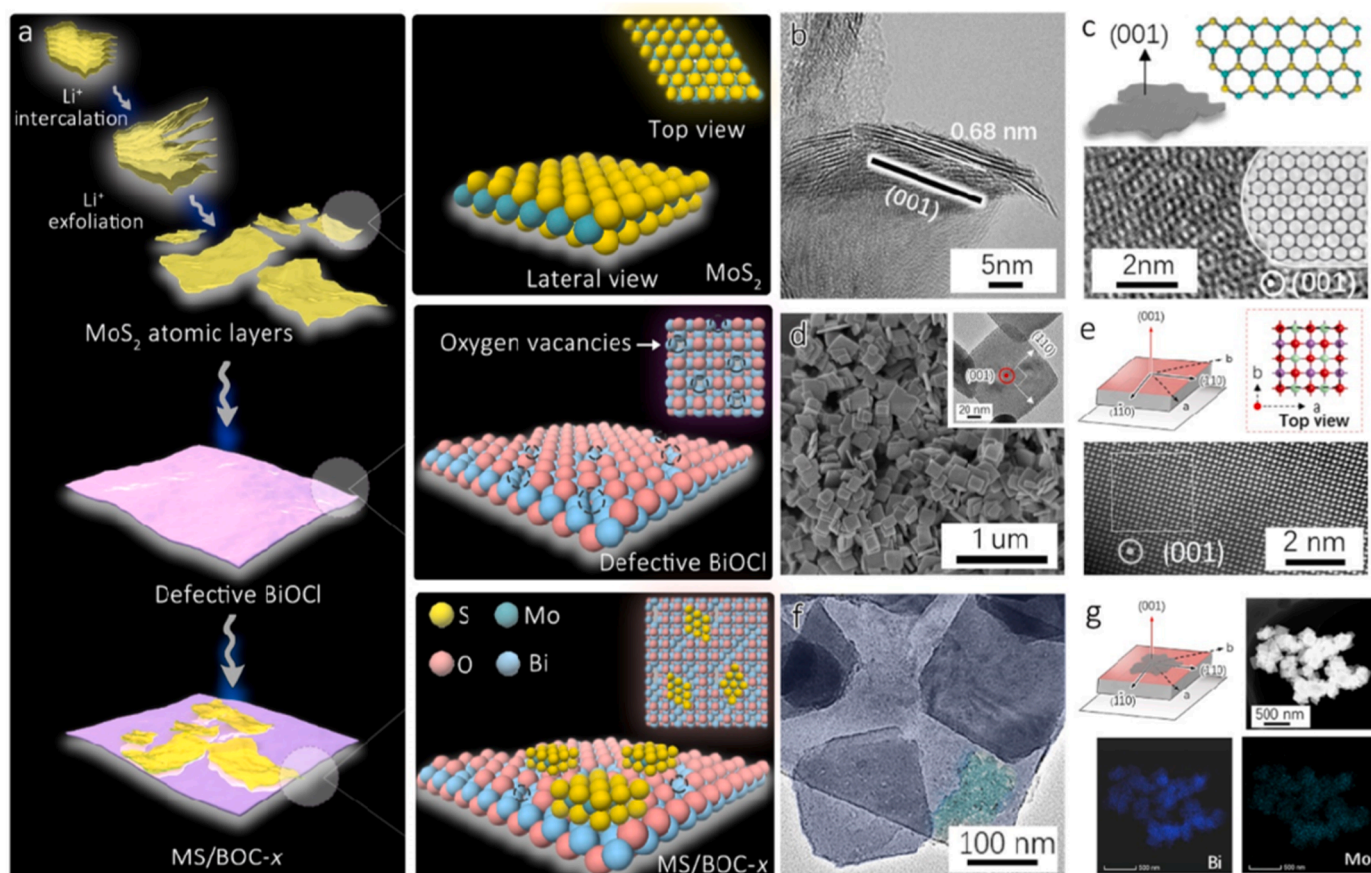
Fig. 1. a) Scheme depicting the synthesis of MS/BOC-x. b, c) TEM and HRTEM images of the lateral and top view of MoS_2 (top view atomic arrangements of MoS_2 are marked in the inset of c). d) TEM images of the defective BiOCl nanosheets. e) HRTEM images of the top view of BiOCl (top view atomic arrangements of BiOCl are marked in the inset of e). f) TEM images and g) EDS elemental maps of MS/BOC-11.5.

BiOCl bases. Generally, {001} surfaces of BiOCl are often covered by charge stabilizing hydroxyls from water or nucleophilic groups from organic solvents [34], restricting the direct interactions through positively charged $[Bi_2–O_2]^{2+}$ layers and negatively charged S^{2-} layers. Thus, designing vacant sites (in stoichiometric BiOCl surface) was the pre-request to achieve MoS_2 loading. By prolonging the Ar treatment time, d-BOC samples containing varying amounts of OV were obtained (Fig. S6). As shown in Fig. 2b, ESR spectra exhibited axial signals with a value of 2.002 (B=300.45 mT), indicating the presence of oxygen vacancies [35]. The intensity of OV-spin slightly decreased after physical MoS_2 mixing, while dropped sharply through chemical MoS_2 loading. Noted that the spin signals were sensitive to local electronic structures, this dramatically diminished g-value suggested that OV in d-BOC were ideally compensated through chemical bonding (Mo or S sites in MoS_2 or residual O_2 in the synthetic system) (Fig. 2b inset). Additionally, the assembly method was also versatile to other systems containing MoX (X = S, Se) (Fig. S7). ESR signals of MoS_2-BiOCl showed a similar OV-related trend to MS/BOC, illustrating that oxygen substitution (in the OV sites of the BOC (001) facet) was critical to hybrid-interfaces (Fig. S8).

Since OV signals vanished through MS loading, chemical states of the reformed MS/BOC interfaces were investigated by X-ray photoelectron spectroscopy (XPS). High-resolution spectra were collected in the Mo 3d, S 2 s, and Bi 4 f regions of MS/BOC-x (x = 2.5, 7.5, 11.5) alongside p-MS/BOC as the reference. As shown in Fig. 2c, the Mo 3d spectra for p-MS/BOC and MS/BOC-11.5 showed two peaks at 232 and 228.8 eV, which could readily be assigned to Mo $3d_{3/2}$ and Mo $3d_{5/2}$ bands of Mo^{4+} [25,36]. The Mo 3d signals of MoS_2 were still well within the range expected for MoO_2 compounds (cf. MoO_2, Mo $3d_{3/2}$ =232.4 eV;

Mo $3d_{5/2}$ = 229.25 eV) [37], thus the fine structure of the Mo site would be discussed later. Fig. 2c also showed S 2 s curves of p-MS/BOC with one peak at 227 eV, while MS/BOC-11.5 could be deconvoluted into two Gaussian peaks at 227 and 225 eV. These two peaks were assigned respectively to SOx species (S^{2-} and partially oxidized surface S in MoS_2) and Bi–S bond [38], verifying the presence of Bi–S interactions. The Bi–S peak regions varied parallel to the MoS_2 loading amount (from MS/BOC-2.5 to 11.5), indicating that Bi-S interactions dominated MS/BOC formation (Fig. 2d). The corresponding Bi 4 f peaks negatively shifted from p-MS/BOC to the MS/BOC-x, identically to S 2 s analyses that explained as a sulfidation of the surface (Fig. S9) [39]. These observations supplemented the aforementioned ESR results, from which the OV sites on the surface of the BOC were probably occupied by S atoms.

To further investigate the coordination environment of Mo atoms in MS/BOC interfaces, Mo K-edge X-ray absorption near-edge structure (XANES), k-space spectra, and extended X-ray absorption fine structure (EXAFS) data were collected for MS/BOC-11.5 and related reference materials. As shown in Fig. S10, the XANES curves for MS/BOC-11.5 displayed a position or white line peak similar to that of MoS_2, indicating Mo atoms in these samples were positively charged with a valence state close to + 4 [40]. The k-space spectra for MS/BOC-11.5 showed oscillations in the pre-edge adsorptions slightly different from MoS_2 (Fig. 2f inset), suggesting that the Mo atoms in MS/BOC-11.5 were partly unconventionally coordinated. The Mo K-edge EXAFS spectra for MS/BOC-11.5 showed one Mo–S shell (1.91 Å) and one Mo–Mo shell (2.86 Å) in the short-range local structure region (below 4 Å), whereas the Mo–O/Mo–Mo shell (1.96 Å; 2.79 Å) belonging to MoO_2 were absent (Fig. 2f and Fig. S10) (The peaks below 1.5 Å originated from Li_xMoS_2
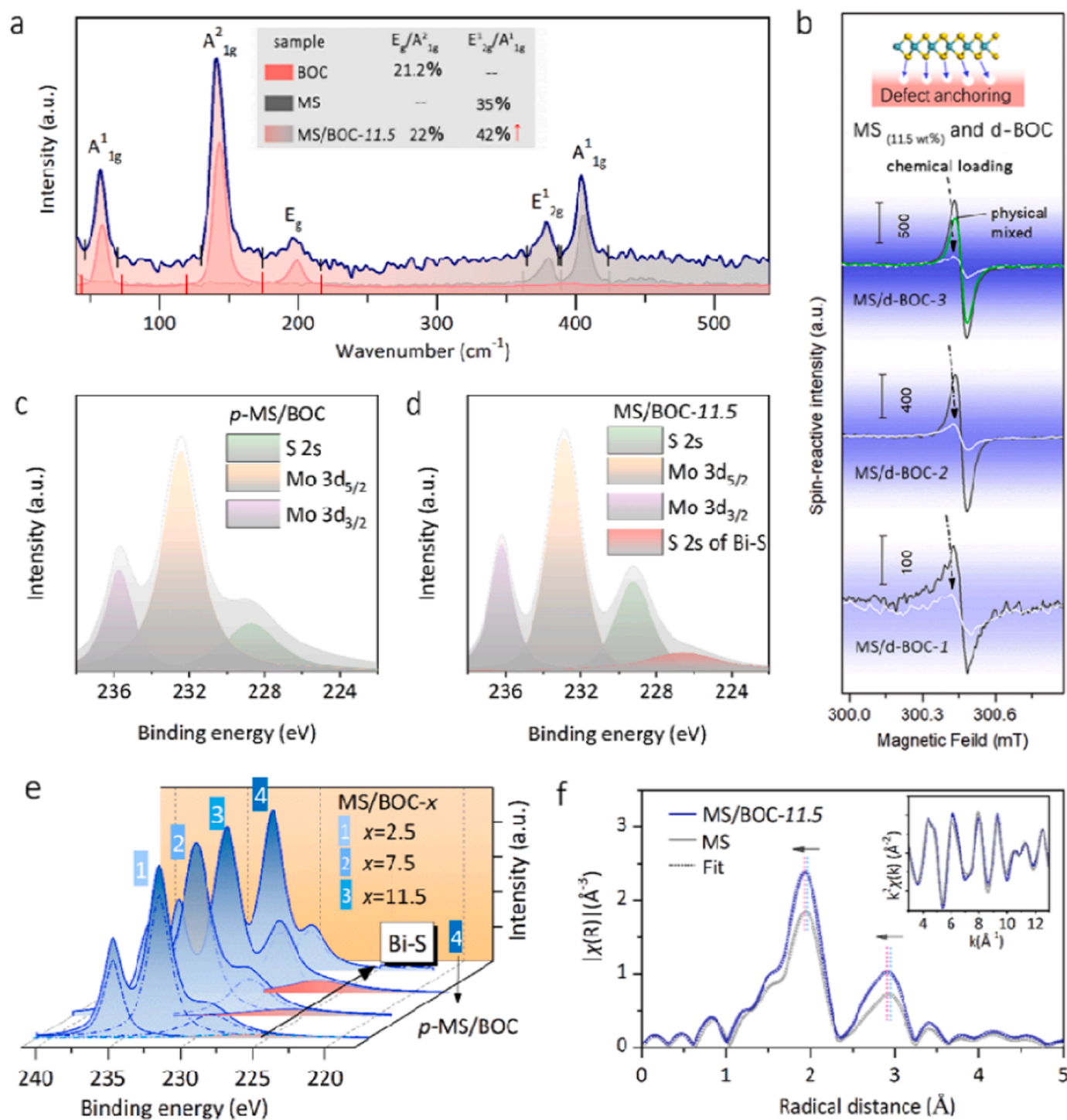
Fig. 2. a) Raman spectra of pristine MoS_2, BiOCl, and MS/BOC-11.5. b) ESR analysis of chemically / physically a mixture of MS and d-BOC. c, d, e) Mo 3d and S 2 s XPS spectra of p-MS/BOC and MS/BOC-x (x = 2.5, 7.5, 11.5). f) Fourier transforms and corresponding fitting results of the Mo K-edge EXAFS spectra for MS and MS / BOC-11.5 (The Mo K-edge EXAFS oscillation functions k3χ (k) of MS and MS/BOC-11.5 are shown in the inset of f).

interactions through the lithium-intercalated/de-intercalated method [41–43]). The curve fitting results revealed that the average coordination number (CN) of Mo atoms in MS/BOC-11.5 was 3.9 (4.8 for MoS_2) with a shrinking Mo–S distance, elucidating the collapse of local MoS_2 structures (after chemical loading) (Table S1). Therefore, based on the XAFS results, Mo–S bond was distorted at the MS/BOC interfaces. Since S atoms have been proven to substitute O atoms in BOC bases from XPS and ESR analysis (by occupying OV sites), a coherent Mo-S-Bi hybrid was thereafter newly generated.

Accordingly, the newly-generated Mo-S-Bi pairs gave a metal-to-metal charge transfer (MMCT) path at MS/BOC interface. Especially for the photocatalytic applications, the light-adsorption, charge-carriers migration and surface catalytic routes were all possibly modulated through Mo-S-Bi bonding. Therefore, to deliver a comprehensive understanding of dipole-induced (symmetry - breaking by Mo-S-Bi bond) photocatalytic processes from an atomic-level, the optical-electrical properties of MS/BOC-11.5, isolated MS and BOC were separately explored. Fig. S11 showed the density functional theory (DFT)

calculations about the total density of states (TDOS) of MS and BOC. The simulated conduction band minimum (CBM) of MS was situated much closer to the Fermi level than that of BOC, readily indicating an electron donation from O 2p to Mo 4d orbitals (BOC to MS). Moreover, the band gap interval of MS was also narrower than that of BOC, which endowed MS with a wide light-response range. Ultraviolet-visible (UV–vis) diffuse reflectance spectra (DRS) visualized the light absorption edges of MS, BOC, and MS/BOC-11.5. Results showed that the isolated BOC provided a maximum UV-light response up to 380 nm, which red-shifted to visible-light region (>420 nm) after MS loading (Fig. 3a) [54,55]. Using the Kubelka–Munk function, the relative band gaps of MS and BOC were determined as 1.4 and 3.3 eV,

and the corresponding valence band (VB) positions were calculated as 0.8 and 1.98 eV (vs. SHE), respectively (Fig. 3b). In addition, the CB levels of MS and BOC were estimated as –0.6 and –1.32 eV (vs SHE), all satisfying the thermodynamic requirements for the reduction of H_2O to H_2 (pH=7) (above the H^+/H_2 couples with only BOC could provide O_2 evolution) (Fig. 3c) [44,45]. Fig. 3a also showed the incident-photon-to-current conversion efficiency (IPCE) of MS and MS/BOC-11.5. The IPCE curve of MS/BOC-11.5 varied parallel with BOC's light absorption tendency, suggesting that BOC dominated photovoltaic conversion. Whereas for bare MoS_2, the IPCE signal was closely to 0, suggesting a weak light-to-current response (probably due

to the rapid charge recombination in MS) (Fig. S12). The irradiation wavelength-dependent apparent quantum efficiency of MS/BOC-11.5 also matched well with the photo-absorption characteristic of BOC (Fig. S13). This observation directly illustrated a charge transfer direction from BOC to MS, which was in good agreement with DFT and band alignments simulations.

To understand photoinduced charge carrier dynamics, open circuit voltage decay (OCVD) was used to monitor in-situ electrical signals of the photocatalysts upon light irradiation. Generally, OCVD is a quasi-equilibrium measurement that preferentially records the slow charge-recombination kinetics (milliseconds–seconds), which lies in the time-scale for surface chemical reactions. A transient photovoltage (Voc) aroused gradually to an equilibrium and then decayed to ground state for all the samples (with/without illumination). During this process, the average lifetime (τ) of photoexcited carriers can be quantified from the Voc decay curves. The calculated τ values increased from 1.87 ms to 4.16 ms for d-BOC-1 and d-BOC-3 samples, suggesting the rapid electron-hole separation at OV sites (Fig. S14). The electron transfer process can be further accelerated through MS loading (chemically/physically), with the maximal τ value exceeding to 27.05 ms (MS/BOC-11.5) (Fig. 3d,e). This clearly verified MMCT paths overwhelmed OV-sites for interfacial charge separation, motivating the design of hybrid 2D materials through defect engineering (Fig. 3f). Moreover, the
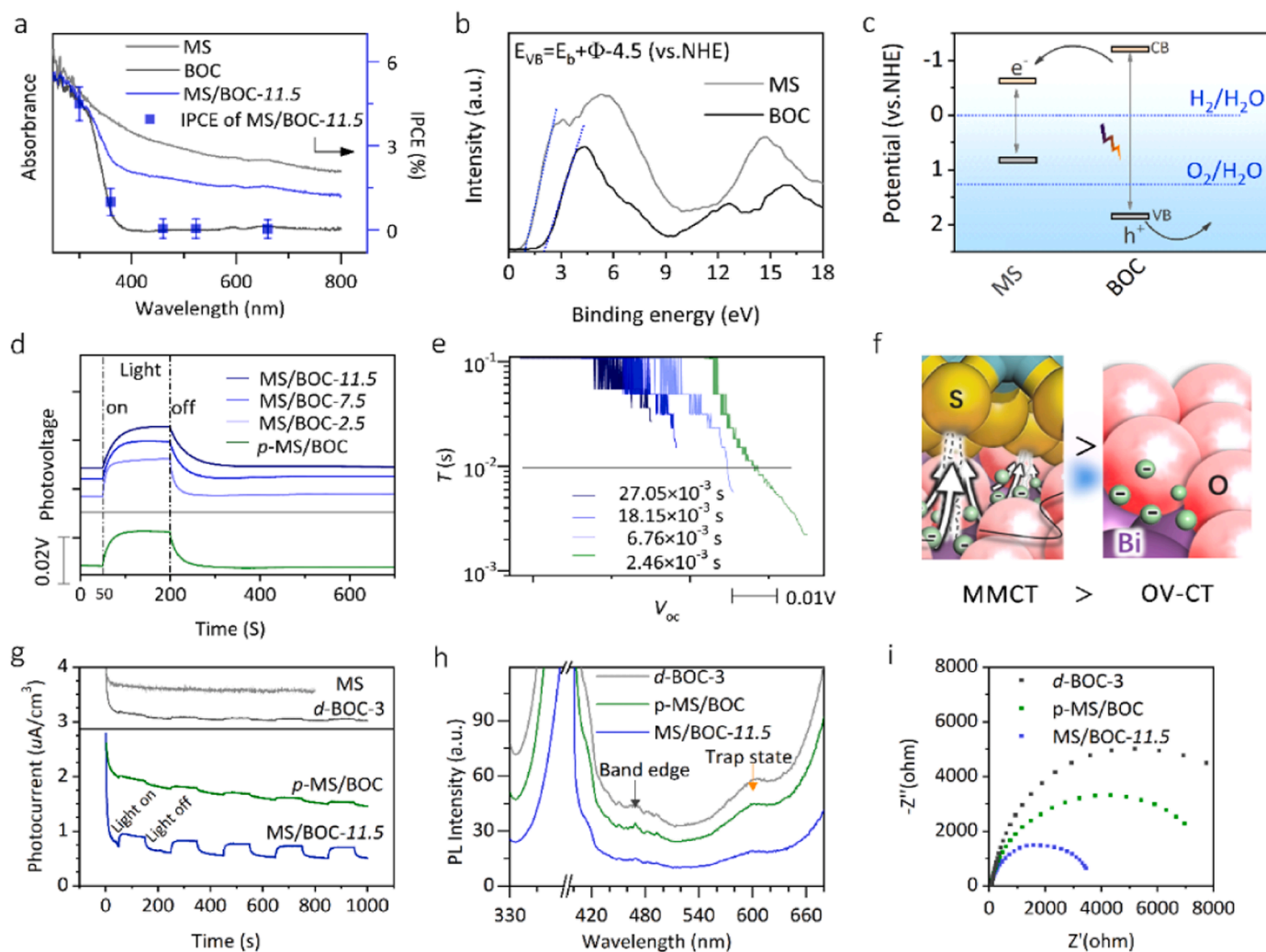

Fig. 3. a) Diffuse reflectance spectra of MS, BOC and MS/BOC-11.5 and incident photon-to-current conversion efficiency (IPCE) plot for MS/BOC-11.5. b) XPS-VB spectra and c) band alignments for MS and BOC. d) Transient open circuit voltage decay and corresponding e) voltage decay curves for p-MS/BOC and MS/BOC-x (x = 2.5, 7.5, 11.5) (excitation at 360 nm). f) Schematic diagrams showing the interface electron-transfer paths over MS/BOC-x and d-BOC. g) Photocurrent response, h) photoluminescence spectra (excited at 320 nm) and i) EIS spectra of d-BOC-3, p-MS/BOC, and MS/BOC-11.5,respectively.

photocurrent signals demonstrated by MS/BOC-11.5 also surpassed all related references, matching well with the above-mentioned IPCE and OCVD results (Fig. 3g). Fig. 3h,i showed photoluminescence (PL) and electrochemical impedance spectroscopy (EIS) of MS/BOC-x samples (x = 2.5, 7.5, 11.5). MS/BOC-11.5 displayed quenched PL signals with the smallest EIS semicircles. Noted the weakened PL peaks reflected the suppressed electron-hole recombination and the EIS radius correlated with the inner-resistance [46], the afore-mentioned results thus collectively indicated MS/BOC-11.5 possessed the best charge.

separation efficiency due to its high conductivity. The long-lived charge carriers gave more opportunities for surface reactions, offering MS/BOC-11.5 a good candidate for photocatalytic applications.

Solar-driven water splitting (photocatalytic water splitting, PWS) is a promising method to achieve artificial photosynthesis, where the efficient separation of electron-hole pairs to redox sites is crucial. Since the

lifetime of photo-excited charge carries in MS/BOC-x was well-within the scope for surface catalytic reactions, the PWS performance of MS/BOC-x was of particular interest. The PWS experiments were performed under neutral conditions (pH≈7, without sacrificial agents) in a Pyrex vessel. Before UV-Vis light irradiation (160 mW cm^{-2}, Xenon lamp), residual air was removed by evacuation and Ar injection (Fig. S15). The gaseous products formed were analyzed by gas chromatography (GC), and the relative yields were quantified through an external standard method. Fig. 4a showed the hydrogen evolution reaction (HER) performance of MS/BOC-x (x = 2.5 to 15). The H_2 release amounts drastically increased to a maximum about 165 μmol·g^{-1} in the first one hour with enlarging MS contents in BOC (from 2.5% to 11.5%). This value almost kept a constant upon further MS loading, suggesting MS/BOC-11.5 was optimal for H_2 production. Fig. 4b further showed d-BOC-3 delivered a H_2 formation rate of 24 μmol·g^{-1}·h^{-1}, much higher
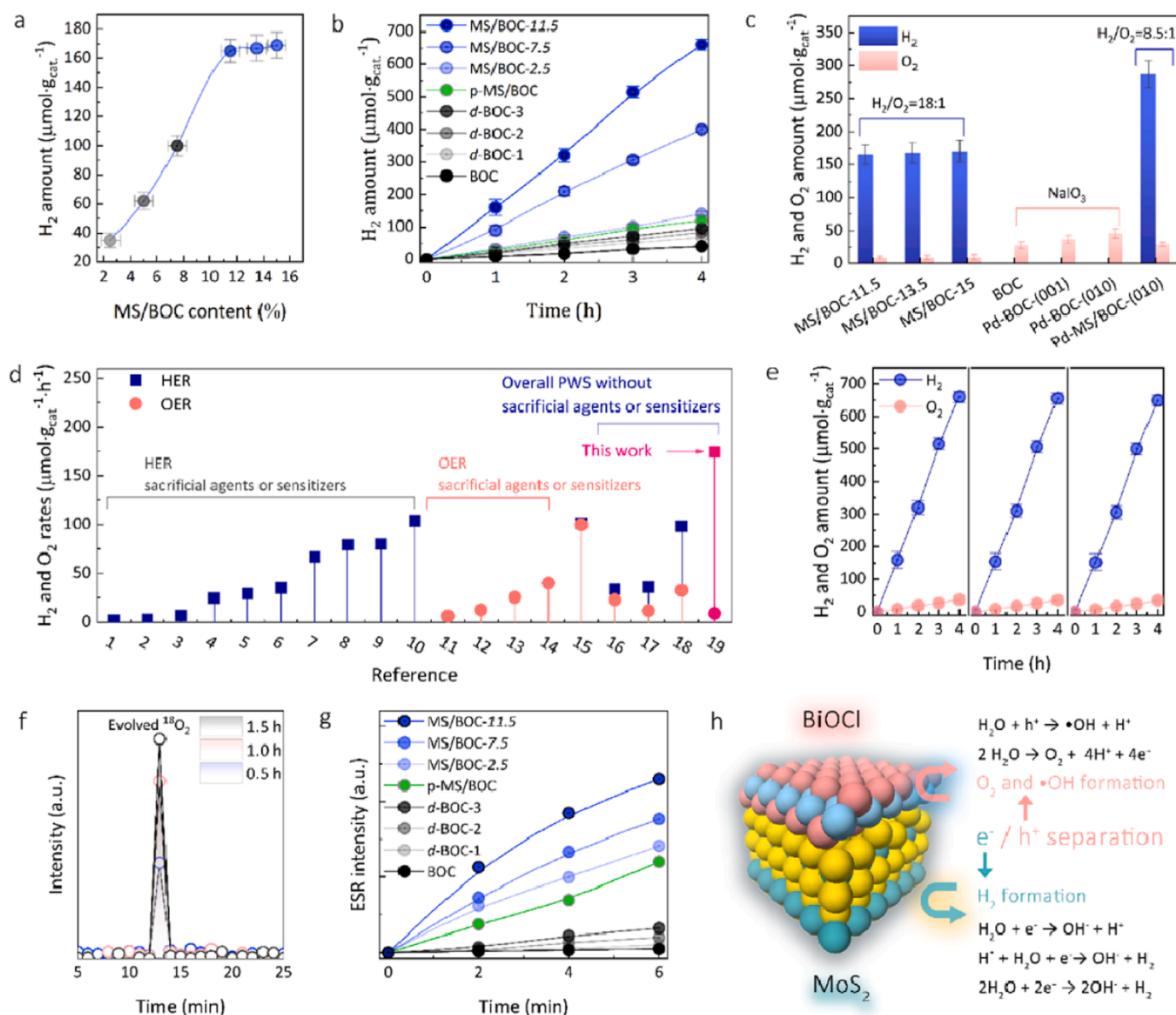

Fig. 4. a) Average amount of hydrogen evolution collected at 1 h over MS/BOC-x (x = 2.5, 5, 7.5, 11.5, 13.5 and 15). b) H_2 yield as a function of reaction time for MS/BOC-x (x = 2.5, 7.5, 11.5), p-MS/BOC, d-BOC (d-BOC-1 to d-BOC-3) and pristine BOC. Reaction condition: 10 mL of H_2O, full spectrum irradiation and 10 mg of catalyst. c) Average amount of hydrogen and oxygen evolution collected at 1 h over MS/BOC-x (x = 11.5, 13.5 and 15), BOC, Pd on the (001)/(010) surfaces of BOC and Pd on the (010) surface of MS/BOC-11.5. d) Performance comparison of various BiOX (X = Cl, Br) based and MoS2 based catalysts with/without the asset capacity of sacrificial agents and photosensitizers. e) Cycle experiments of overall water splitting performance for MS/BOC-11.5. f) $^{18}O_2$ mass spectrum produced by the photoreduction of $H_2^{18}O$ MS/BOC-11.5. g) ESR signals of •OH radicals generated from MS/BOC-x (x = 2.5, 7.5, 11.5), p-MS/BOC, d-BOC (d-BOC-1 to d-BOC-3) and pristine BOC. h) Scheme showing the OER/HER positions in the MS/BOC hybrid.

than that of BOC (10 µmol·g^{-1}·h^{-1}). After the introduction of MS, the HER activity was remarkably improved. MS/BOC-11.5 offered the highest H$_2$ evolution rate of 165 µmol·g^{-1}·h^{-1}, which was 1.65, 2.36 and 4.71 times higher than the activities of MS/BOC-7.5, MS/BOC-2.5 and p-MS/BOC reference photocatalysts, respectively. The slopes of HER rates demonstrated by MS/BOC-x surpassed that of d-BOC samples, suggesting a favorable HER kinetics through MS loading. This enhanced HER performance might be attributed to the promoted reduction half reaction relying on fast charge transfer, as well as MS provided extra active sites for H$_2$O-to-H$_2$ conversion. Meanwhile, oxygen evolution reaction (OER) performance was simultaneously explored. As shown in Fig. 4c, MS/BOC-11.5, MS/BOC-13.5 and MS/BOC-15 were all active for O$_2$ formation, with the rates of O$_2$ approximately 9.17 µmol·g^{-1}·h^{-1}. The H$_2$/O$_2$ fraction was determined as 18:1, far beyond the stoichiometric ratio for ideal water dissociation (H$_2$/O$_2$ = 2:1). This clearly implied HER and OER reactivities were different over MS/BOC samples, which probably due to unequally redox capacities upon diverse surface sites. For example, when equivalent Pd nanocubes were loaded separately on

the top (001 facet) or lateral facets (010/110 facet) of BOC, the activity of O$_2$ production changed greatly (Fig. 4c and Fig. S16). By rationally designing Pd nanocubes on the lateral facets (010/110 facet) of MS/BOC-11.5 (Pd-MS/BOC-11.5, without altering the intrinsic structure of the MS/BOC-11.5 and MMCT paths), the H$_2$ and O$_2$ production rates (287 µmol·g^{-1}·h^{-1} and 33.5 µmol·g^{-1}·h^{-1}, respectively) especially the H$_2$/O$_2$ ratio (8.5:1) were immediately modified (Fig. 4c and Fig. S17). This suggested that the (010) facet of BOC preferred OER over its (001) facet, consistent with previously reported works [47]. The overall water splitting activity (especially HER) demonstrated by MS/BOC-11.5 was comparable to other state-of-the-art heterogeneous catalysts involving either MS or BOC, with the advantage that no sacrificial agents or sensitizers were required (Fig. 4d and Table S2). Cycle experiments were subsequently conducted to explore the stability of MS/BOC-11.5 (Fig. 4e). Furthermore, a comparative analysis before and after the reaction suggests that the crystal structure of MS/BOC-11.5 remains largely unaffected by the illumination exposure (Fig. S18,19,20). No obviously decrease in the H$_2$/O$_2$ production rate was observed over
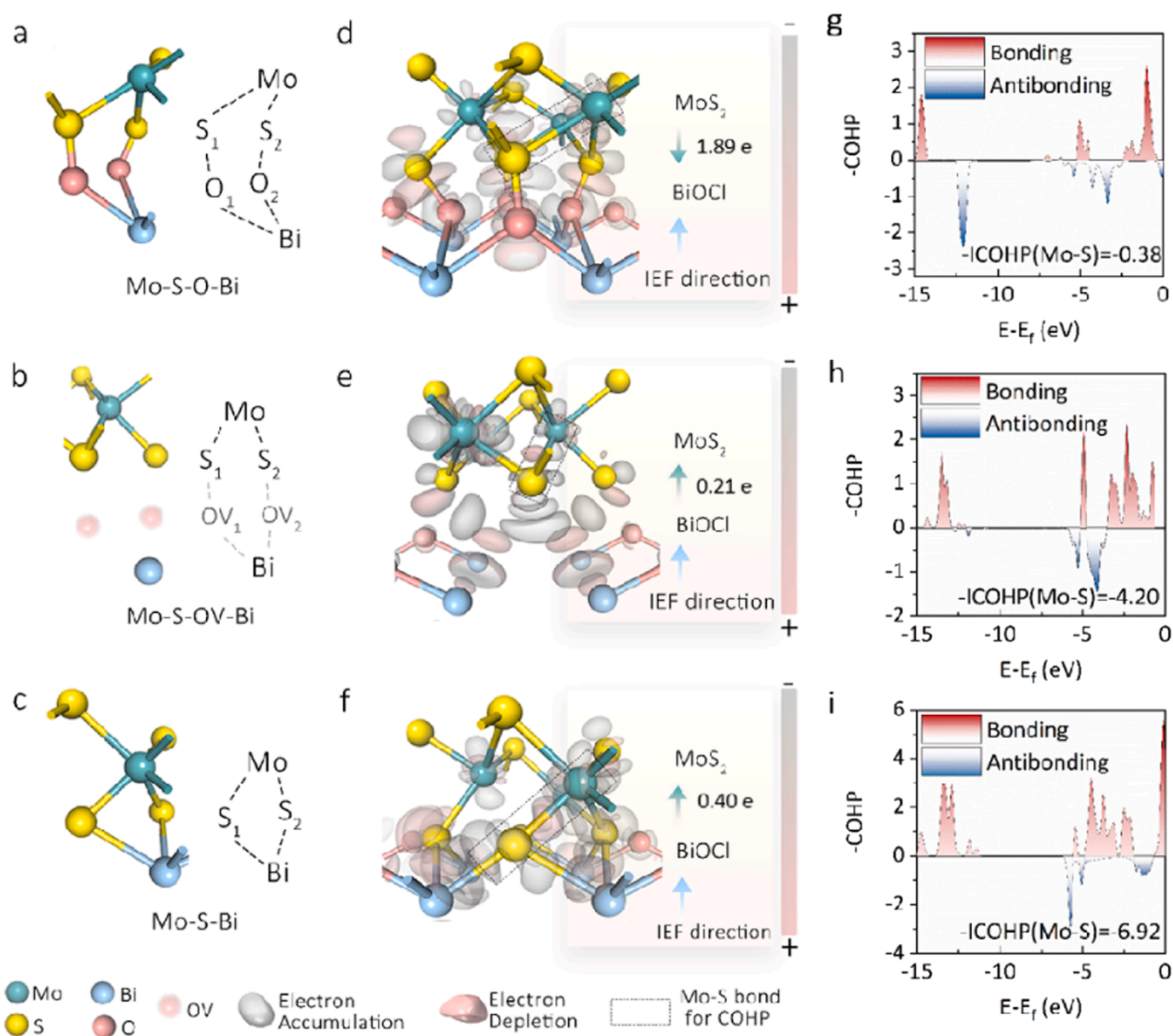
Fig. 5. a-c) Theoretical geometries, d-f) the corresponding differential charge density diagrams and g-i) the ICOHP plots of the Mo-S bond in Mo-S-O-Bi, Mo-S-OV-Bi and Mo-S-Bi models based on the atomic arrangement on the (001) surface of BiOCl and MoS$_2$.

three testing cycles, indicating that the photocatalyst possessed good photostability. Isotopic labeling experiments confirmed that H_2O was indeed the oxygen source leading to O_2, with the amount of 18 $_{O_2}$ continuously increasing with irradiation time (Fig. 4f).

Actually, reactive oxygen species (ROS) especially •OH radical was also the by-product during O_2 production. Time-resolved ESR spectra was performed to trace the photo-induced •OH radical. In each test, equal amounts of catalysts were collected and afterwards operated in 77 K to shield the background noise. Fig. S21 showed regularly four-line ESR signals with relative intensities of 1:2:2:1 over d-BOC-3 and MS/BOC-11.5, proving the generation of •OH radical [48]. The ESR peak intensified from d-BOC-3 to MS/BOC-11.5 until a uppermost •OH generation slope (k, min^{-1}) nearly 190 min^{-1}, suggesting MS/BOC-11.5 preferred water oxidation (Fig. 4g and Fig. S22). Noted •OH radical was the outcome from photo-induced holes ($H_2O + h^+ \rightarrow \bullet OH + H^+$) [49–51], this observation thus implied that MS/BOC-11.5 benefited h^+ utilization/migration (along with e- separation). The surface adsorbed OH was the intermediate related to O_2 formation, while the consumption of OH to •OH radical (rather than OH to O_2) and •OH back to H_2O wasted excessive h^+ thus resulted in a non-stoichiometric H_2/O_2 ratio (Fig. 4h). Another possible reason is that slight photo-corrosion of MoS_2 occurs due to the production of reactive oxygen species (ROS) during photocatalytic water oxidation (Table S3).

To gain a deeper understanding of the charge transfer processes at an atomic level, we conducted a systematic analysis of DFT calculations of the MS/BOC interfaces. Based on the aforementioned HRTEM, ESR, and XAFS studies, we constructed surface models with electrostatically interacted [Bi-O]$^{2+}$-S^{2-} bilayers (Mo-S-O-Bi), S-OV intercalated MS/BOC (Mo-S-OV-Bi), and S-bridged MS/BOC (Mo-S-Bi) (Fig. 5a-c). Charge migration path of BiOCl during MoS_2 loading was provided by the differential charge density diagrams shown in Fig. 5d-f [47]. The corresponding Bader charge calculation showed that electrons of 1.89 e were donated from MoS_2 to BiOCl within the Mo-S-O-Bi model, whilst electrons of 0.21 e and 0.40 e were transferred from BiOCl to MoS_2 for the Mo-S-OV-Bi and Mo-S-Bi models. This clearly illustrated that Mo-S-Bi preferred BOC-to-MS electron donation, integrating the inner electron migration of BiOCl (through the [001] direction) as well as enlarging interfacial charge overlaps. Additionally, the crystal orbital Hamiltonian population (COHP) analyses were further adopted (Fig. 5g-i) [52]. The absolute values of the integrated COHP (ICOHP) of the Mo-S bond increased from Mo-S-O-Bi to Mo-S-Bi, indicating that the Mo-S bond gradually strengthened [53]. This could be ascribed to the bridged S atoms, which maximized electronic hybridization near the hybrid interfaces and improved the chemical stability of MoS_2 during use. The Mo-S-Bi model appeared to closely mimic the interfacial properties of the MS/BOC-11.5 photocatalyst, fully accounting for its remarkable HER/OER activity for overall water splitting.

4. Conclusions

In summary, MS/BOC-11.5 photocatalyst consisting of uniformly dispersed MoS_2 atomic layers over a defective BiOCl support yielded excellent performance for general water splitting to H_2 and O_2 under UV-Vis irradiation. The oxygen vacancies in the (001) facet of BiOCl provided anchoring sites to immobilize MoS_2 through a Mo-S-Bi bonding, thus creating a new charge transfer path at the MS/BOC interface. Benefiting from the MMCT configuration, the aqueous medium achieved a photoinduced H_2 formation rate of 165 μmol·g^{-1}·h^{-1}, which was at least 5.5 and 16.5 times higher than that of defective BiOCl and perfect BiOCl, respectively. Furthermore, the O_2 production rate of MS/BOC-11.5 was estimated to be 9.17 μmol·g^{-1}·h^{-1}, with properly adsorbed surface OH as the reaction intermediate. The collectively water splitting performance peculiarly HER rates reported here were superior to many states of the art MoS_2 or BiOCl-involved homogeneous/hybrid catalysts, especially the usage of sacrificial agents or sensitizers were avoided in present PWS system. DFT calculations

showed that the surface charge overlaps demonstrated by Mo-S-Bi pairs outperformed those of the Mo-S-OV-Bi and Mo-S-O-Bi interfaces, integrating the inner/interfacial electron injection from BiOCl to MoS_2 thereby realizing efficient e$^-$/h$^+$ separation. Therefore, the MS/BOC-11.5 photocatalyst achieved unusually high H_2/O_2 production rates during the PWS tests reported herein. Our findings provide insights into the rational design of hybrid photocatalysts with highly efficient operation for the overall/half-water splitting reaction.

Author contributions

B. S., C. H. and C. Y. designed the experiments and drafted the manuscript; D. K. analyzed the data and contributed to creating the images; Y. L. performed the DFT calculations; Q. L. and X. L. participated in analyzing and discussing the characterization data; X. X., Y. C., Q. J., J. H. and T. Z. conceived the project, provided guidance and supervision throughout the work. All authors have approved the manuscript.

CRediT authorship contribution statement

Zhou Tengfei: Funding acquisition, Investigation, Project administration, Resources, Supervision, Writing – original draft, Writing – review & editing. **Jiang Qingqing:** Formal analysis, Methodology. **Hu Juncheng:** Funding acquisition, Supervision. **Sun Bingjie:** Data curation, Investigation, Methodology. **Lu Qi:** Methodology, Writing – review & editing. **Liu Xiufan:** Data curation, Resources. **Xiong Xuyang:** Funding acquisition, Supervision, Writing – review & editing. **Chen Yuanzhen:** Investigation, Resources, Writing – review & editing. **Huang Cheng:** Conceptualization, Data curation, Formal analysis, Investigation, Writing – original draft. **Yang Chenyu:** Investigation, Visualization, Writing – review & editing. **Ke Da:** Methodology, Visualization. **Liu Ye:** Data curation, Investigation, Software, Writing – review & editing.

Declaration of Competing Interest

The authors declare that they have no known competing financial interests or personal relationships that could have appeared to influence the work reported in this paper.

Data availability

Data will be made available on request.

Acknowledgements

Appendix A. Supporting information

Supplementary data associated with this article can be found in the online version at doi:10.1016/j.apcatb.2024.123720.

References

[1] X. Tao, H. Zhou, C. Zhang, N. Ta, R. Li, C. Li, Triclinic-phase bismuth chromate: a promising candidate for photocatalytic water splitting with broad spectrum ranges, Adv. Mater. 35 (2023) 2211182.

[2] X. Xin, Y. Zhang, R. Wang, Y. Wang, P. Guo, X. Li, Hydrovoltaic effect-enhanced photocatalysis by polyacrylic acid/cobaltous oxide–nitrogen doped carbon system for efficient photocatalytic water splitting, Nat. Commun. 14 (2023) 1759.

[3] M. Ashraf, N. Ullah, I. Khan, W. Tremel, S. Ahmad, M. Tahir, Photoreforming of waste polymers for sustainable hydrogen fuel and chemicals feedstock: waste to energy, Chem. Rev. 123 (2023) 4443–4509.

[4] H. Liu, M. Cheng, Y. Liu, J. Wang, G. Zhang, L. Li, L. Du, G. Wang, S. Yang, X. Wang, Single atoms meet metal–organic frameworks: collaborative efforts for efficient photocatalysis, Energy Environ. Sci. 15 (2022) 3722–3749.

[5] Y. Wang, D. Xie, G. Wang, Y. Wu, R. Shi, C. Zhao, X. Meng, T. Zhang, Single-atomic Co-N$_4$-O site boosting exciton dissociation and hole extraction for improved photocatalytic hydrogen evolution in crystalline carbon nitride, Nano Energy 104 (2022) 107938.

[6] M. Qi, M. Conte, M. Anpo, Z. Tang, Y. Xu, Cooperative coupling of oxidative organic synthesis and hydrogen production over semiconductor-based photocatalysts, Chem. Rev. 121 (2021) 13051–13085.

[7] X. Tao, Y. Zhao, S. Wang, C. Li, R. Li, Recent advances and perspectives for solar-driven water splitting using particulate photocatalysts, Chem. Soc. Rev. 51 (2022) 3561–3608.

[8] T. Suguro, F. Kishimoto, N. Kariya, T. Fukui, M. Nakabayashi, N. Shibata, T. Takata, K. Domen, K. Takanabe, A hygroscopic nano-membrane coating achieves efficient vapor-fed photocatalytic water splitting, Nat. Commun. 13 (2022) 5698.

[9] Y. Yang, S. Zhao, F. Bi, J. Chen, Y. Wang, L. Cui, J. Xu, X. Zhang, Highly efficient photothermal catalysis of toluene over Co$_3$O$_4$/TiO$_2$ p-n heterojunction: The crucial roles of interface defects and band structure, Appl. Catal. B: Environ. 315 (2022) 121550.

[10] Y. Wang, H. Suzuki, J. Xie, O. Tomita, D.J. Martin, M. Higashi, D. Kong, R. Abe, J. Tang, Mimicking natural photosynthesis: solar to renewable H$_2$ fuel synthesis by Z-scheme water splitting systems, Chem. Rev. 118 (2018) 5201–5241.

[11] F. Chen, T. Ma, T. Zhang, Y. Zhang, H. Huang, Atomic-level charge separation strategies in semiconductor-based photocatalysts, Adv. Mater. 33 (2021) 2005256.

[12] Y. Wang, A. Vogel, M. Sachs, R. Sprick, L. Wilbraham, S. Moniz, R. Godin, M. A. Zwijnenburg, J. Durrant, A. Cooper, J. Tan, Current understanding and challenges of solar-driven hydrogen generation using polymeric photocatalysts, Nat. Energy 4 (2019) 746–760.

[13] H. Zhou, Y. Qu, T. Zeid, X. Duan, Towards highly efficient photocatalysts using semiconductor nanoarchitectures, Energy Environ. Sci. 5 (2012) 6732–6743.

[14] R. Marschall, Semiconductor composites: strategies for enhancing charge carrier separation to improve photocatalytic activity, Adv. Funct. Mater. 24 (2014) 2421–2440.

[15] E. Gong, S. Ali, C. Hiragond, H. Kim, N. Powar, D. Kim, H. Kim, S. In, Solar fuels: research and development strategies to accelerate photocatalytic CO$_2$ conversion into hydrocarbon fuels, Energy Environ. Sci. 15 (2022) 880–937.

[16] X. Wang, C. Liow, A. Bisht, X. Liu, T. Sum, X. Chen, S. Li, Engineering interfacial photo-induced charge transfer based on nano-bamboo array architecture for efficient solar-to-chemical energy conversion, Adv. Mater. 27 (2015) 2207–2214.

[17] Y. Zhao, G. Waterhouse, G. Chen, X. Xiong, L. Wu, C. Tung, T. Zhang, Two-dimensional-related catalytic materials for solar-driven conversion of COx into valuable chemical feedstocks, Chem. Soc. Rev. 48 (2019) 1972–2010.

[18] Y. Lin, C. Yang, S. Wu, X. Li, Y. Chen, W.L. Yang, Construction of built-in electric field within silver phosphate photocatalyst for enhanced removal of recalcitrant organic pollutants, Adv. Funct. Mater. 30 (2020) 2002918.

[19] L. Zhai, X. She, L. Zhuang, Y. Li, R. Ding, X. Guo, Y. Zhang, Y. Zhu, K. Xu, H. Fan, Modulating built-in electric field via variable oxygen affinity for robust hydrogen evolution reaction in neutral media, Angew. Chem. Int. Ed. 134 (2022) e202116057.

[20] J. Di, C. Chen, S. Yang, M. Ji, C. Yan, K. Gu, J. Xia, H. Li, S. Li, Z. Liu, Defect engineering in atomically-thin bismuth oxychloride towards photocatalytic oxygen evolution, J. Mater. Chem. A 5 (2017) 14144–14151.

[21] D. Cui, L. Wang, K. Xu, L. Ren, L. Wang, Y. Yu, Y. Du, W. Hao, Band-gap engineering of BiOCl with oxygen vacancies for efficient photooxidation properties under visible-light irradiation, J. Mater. Chem. A 6 (2018) 2193–2199.

[22] H. Li, J. Li, Z. Ai, F. Jia, L. Zhang, Oxygen vacancy-mediated photocatalysis of BiOCl: reactivity, selectivity, and perspectives, Angew. Chem., Int. Ed. 57 (2018) 122–138.

[23] H. Karunadasa, E. Montalvo, Y. Sun, M. Majda, J. Long, C. Chang, A molecular MoS$_2$ edge site mimic for catalytic hydrogen generation, Science 335 (2012) 698–702.

[24] J. Li, G. Zhan, Y. Yu, L. Zhang, Superior visible light hydrogen evolution of Janus bilayer junctions via atomic-level charge flow steering, Nat. Commun. 7 (2016) 11480.

[25] P. Wang, H. Sun, Y. Ji, W. Li, X. Wang, Three-dimensional assembly of single-layered MoS$_2$, Adv. Mater. 26 (2014) 964–969.

[26] Z. Wu, J. Shen, W. Li, J. Li, D. Xia, D. Xu, S. Zhang, Y. Zhu, Electron self-sufficient core-shell BiOCl @ Fe-BiOCl nanosheets boosting Fe (III) / Fe (II) recycling and synergetic photocatalysis-Fenton for enhanced degradation of phenol, Appl. Catal., B 330 (2023) 122642.

[27] M. Guan, C. Xiao, J. Zhang, S. Fan, R. An, Q. Cheng, J. Xie, M. Zhou, B. Ye, Y. Xie, Vacancy associates promoting solar-driven photocatalytic activity of ultrathin bismuth oxychloride nanosheets, J. Am. Chem. Soc. 135 (2013) 10411–10417.

[28] J. Li, K. Zhao, Y. Yu, L. Zhang, Facet-level mechanistic insights into general homogeneous carbon doping for enhanced solar-to-hydrogen conversion, Adv. Funct. Mater. 25 (2015) 2189–2201.

[29] B. Gao, J. Zhang, L. Chen, J. Guo, S. Shen, C. Au, S. Yin, M. Cai, Density functional theory calculation on two-dimensional MoS$_2$/BiOX (X= Cl, Br, I) van der Waals heterostructures for photocatalytic action, Appl. Surf. Sci. 492 (2019) 157–165.

[30] J. Di, J. Xiong, H. Li, Z. Liu, Ultrathin 2D photocatalysts: electronic-structure tailoring, hybridization, and applications, Adv. Mater. 30 (2018) 1704548.

[31] P. Pham, S.C. Bodepudi, K. Shehzad, Y. Liu, Y. Xu, B. Yu, X. Duan, 2D heterostructures for ubiquitous electronics and optoelectronics: principles, opportunities, and challenges, Chem. Rev. 122 (2022) 6514–6613.

[32] H. Wang, S. Chen, D. Yong, X. Zhang, S. Li, W. Shao, X. Sun, B. Pan, Y. Xie, Giant electron–hole interactions in confined layered structures for molecular oxygen activation, J. Am. Chem. Soc. 139 (2017) 4737–4742.

[33] D. Kong, H. Wang, J. Cha, M. Pasta, K. Koski, J. Yao, Y. Cui, Synthesis of MoS$_2$ and MoSe$_2$ films with vertically aligned layers, Nano Lett. 13 (2013) 1341–1347.

[34] X. Xiong, L. Ding, Q. Wang, Y. Li, Q. Jiang, J. Hu, Synthesis and photocatalytic activity of BiOBr nanosheets with tunable exposed {0 1 0} facets, Appl. Catal., B 188 (2016) 283–291.

[35] Y. Yang, L. Yin, Y. Gong, P. Niu, J. Wang, L. Gu, X. Chen, G. Liu, L. Wang, H. Cheng, An unusual strong visible-light absorption band in red anatase TiO$_2$ photocatalyst induced by atomic hydrogen-occupied oxygen vacancies, Adv. Mater. 30 (2018) 1704479.

[36] X. Zong, H. Yan, G. Wu, G. Ma, F. Wen, L. Wang, C. Li, Enhancement of photocatalytic H$_2$ evolution on CdS by loading MoS$_2$ as cocatalyst under visible light irradiation, J. Am. Chem. Soc. 130 (2008) 7176–7177.

[37] T. Schroeder, J. Zegenhagen, N. Magg, B. Immaraporn, H. Freund, Formation of a faceted MoO$_2$ epilayer on Mo (1 1 2) studied by XPS, UPS and STM, Surf. Sci. 552 (2004) 85–97.

[38] J.W. Thomson, L. Cademartiri, M. MacDonald, S. Petrov, G. Calestani, P. Zhang, G. Ozin, Ultrathin Bi$_2$S$_3$ nanowires: surface and core structure at the cluster-nanocrystal transition, J. Am. Chem. Soc. 132 (2010) 9058–9068.

[39] Y. Shi, X. Xiong, S. Ding, X. Liu, Q. Jiang, J. Hu, In-situ topotactic synthesis and photocatalytic activity of plate-like BiOCl/2D networks Bi$_2$S$_3$ heterostructures, Appl. Catal., B 220 (2018) 570–580.

[40] Y. Liu, Y. Chen, Y. Tian, T. Sakthivel, H. Liu, S. Guo, H. Zeng, Z. Dai, Synergizing hydrogen spillover and deprotonation by the internal polarization field in a MoS$_2$/NiPS$_3$ vertical heterostructure for boosted water electrolysis, Adv. Mater. 34 (2022) 2203615.

[41] T. Ressler, O. Timpe, T. Neisius, J. Find, G. Mestl, M. Dieterle, R. Schlogl, 2000. J. Catal. 191, 75.

[42] T. Ressler, J. Wienold, R. Jentoft, O. Timpe, T. Neisius, Solid state kinetics of the oxidation of MoO$_2$ investigated by time-resolved X-ray absorption spectroscopy, Solid State Commun. 119 (2001) 169–174.

[43] Z. Zhu, S. Xi, L. Miao, Y. Tang, Y. Zeng, H. Xia, Z. Lv, W. Zhang, X. Ge, H. Zhang, Unraveling the formation of amorphous MoS$_2$ nanograins during the electrochemical delithiation process, Adv. Funct. Mater. 29 (2019) 1904843.

[44] S. Dai, E. Montero-Lanzuela, A. Tissot, H. Baldoví, H. García, S. Navalón, C. Serre, Room temperature design of Ce (iv)-MOFs: from photocatalytic HER and OER to overall water splitting under simulated sunlight irradiation, Chem. Sci. 14 (2023) 3451–3461.

[45] Y. Gao, W. Nie, X. Wang, F. Fan, C. Li, Advanced space-and time-resolved techniques for photocatalyst studies, Chem. Commun. 56 (2020) 1007–1021.

[46] X. Xiong, C. Mao, Z. Yang, Q. Zhang, G. Waterhouse, L. Gu, T. Zhang, Photocatalytic CO$_2$ reduction to CO over Ni single atoms supported on defect-rich zirconia, Adv. Energy Mater. 10 (2020) 2002928.

[47] H. Li, J. Shang, H. Zhu, Z. Yang, Z. Ai, L. Zhang, Oxygen vacancy structure associated photocatalytic water oxidation of BiOCl, ACS Catal. 6 (2016) 8276–8285.

[48] Y. Nosaka, A. Nosaka, Generation and detection of reactive oxygen species in photocatalysis, Chem. Rev. 117 (2017) 11302–11336.

[49] P. Salvador, On the nature of photogenerated radical species active in the oxidative degradation of dissolved pollutants with TiO$_2$ aqueous suspensions: a revision in the light of the electronic structure of adsorbed water, J. Phys. Chem. C. 111 (2007) 17038–17043.

[50] J. Montoya, J. Velasquez, P. Salvador, The direct–indirect kinetic model in photocatalysis: a reanalysis of phenol and formic acid degradation rate dependence on photon flow and concentration in TiO$_2$ aqueous dispersions, Appl. Catal. B: Environ. 88 (2009) 50–58.

[51] J. Schneider, M. Matsuoka, M. Takeuchi, J. Zhang, Y. Horiuchi, M. Anpo, D. Bahnemann, Understanding TiO$_2$ photocatalysis: mechanisms and materials, Chem. Rev. 114 (2014) 9919–9986.

[52] Q. Dang, H. Lin, Z. Fan, L. Ma, Q. Shao, Y. Ji, F. Zheng, S. Geng, S. Yang, N. Kong, Iridium metallene oxide for acidic oxygen evolution catalysis, Nat. Commun. 12 (2021) 6007.

[53] X. Cao, A. Huang, C. Liang, H. Chen, T. Han, R. Lin, Q. Peng, Z. Zhuang, R. Shen, H. Chen, Engineering lattice disorder on a photocatalyst: photochromic BiOBr nanosheets enhance activation of aromatic C–H bonds via water oxidation, J. Am. Chem. Soc. 144 (2022) 3386–3397.

[54] J. Wang, J. Wang, R. Shi, C. Zhou, T. Zhang, Facile fabrication of N-doped K$_2$Nb$_2$O$_6$ nanocrystals with defective pyrochlore structure for improved visible-light photocatalytic hydrogen production, Small Struct. 4 (2023) 2200105.

[55] C. Zhou, T. Wang, D. Li, J. Wang, R. Shi, T. Zhang, Flux-assisted low temperature synthesis of SnNb$_2$O$_6$ nanoplates with enhanced visible light driven photocatalytic H$_2$-production, J. Phys. Chem. C 125 (2021) 23219–23225.